

Reaction-induced Ni-based interstitial carbon atoms for coke-free dry reforming of methane

Qianqian Wang

Taiyuan University of Technology

Wu Wang

Southern University of Science and Technology

Sha Li

Taiyuan University of Technology

Min Cao

Taiyuan University of Technology

Pengfei Wang

Chinese Academy of Sciences

Jiaqing He

Southern University of Science and Technology

Xiaoliang Yan (✉ yanxiaoliang@tyut.edu.cn)

Taiyuan University of Technology <https://orcid.org/0000-0002-6860-4770>

Ruifeng Li

Taiyuan University of Technology

Article

Keywords: synthesis gas, coke deposition, nickel octahedral sites

Posted Date: September 14th, 2021

DOI: <https://doi.org/10.21203/rs.3.rs-753881/v1>

License:   This work is licensed under a Creative Commons Attribution 4.0 International License.

[Read Full License](#)

1 **Reaction-induced Ni-based interstitial carbon atoms for coke-free dry reforming**
2 **of methane**

3 Qianqian Wang^{1,+}, Wu Wang^{2,+}, Sha Li¹, Min Cao¹, Pengfei Wang³, Jiaqing He²,
4 Xiaoliang Yan^{1,4,*}, Ruifeng Li^{1,4}

5 ¹College of Chemistry and Chemical Engineering, Taiyuan University of Technology,
6 Taiyuan, Shanxi, 030024, P. R. China. ² Department of Physics, Southern University
7 of Science and Technology, Shenzhen, Guangdong, 518055, P. R. China. ³State Key
8 Laboratory of Clean and Efficient Coal Utilization, Institute of Coal Chemistry,
9 Chinese Academy of Sciences, Taiyuan, Shanxi, 030001, P. R. China. ⁴Key
10 Laboratory of Coal Science and Technology of Ministry of Education and Shanxi
11 Province, Taiyuan University of Technology, Taiyuan, Shanxi 030024, P. R. China.

12 These authors contributed equally: Qianqian Wang and Wu Wang.

13 Corresponding author, *e-mail: yanxiaoliang@tyut.edu.cn.

14

15 **Abstract**

16 Dry reforming of methane on Ni-based catalyst offers an environmentally and
17 economically viable and pivotal route to produce synthesis gas. The accumulation and
18 polymerization of carbon atoms on the surface of Ni eventually deactivate the catalyst
19 because of coke deposition. Here, we establish a reaction-induced method to isolate
20 carbon atoms into the interstitial position of nickel octahedral sites (O-sites) under
21 reaction condition, which can avoid the C–C bond formation. Al₂O₃ encapsulated
22 Ni₃Zn provides expanded space volume of O-sites in nickel to accommodate carbon
23 atoms, and the further transformation to Ni₃ZnC_{0.7} with superstructure feature was
24 achieved under CH₄/CO₂ reaction. Ni₃ZnC_{0.7}/Al₂O₃ exhibits excellent activity and
25 stability below 600°C with variable CH₄/CO₂ ratio (1/4–2/1). These active carbon

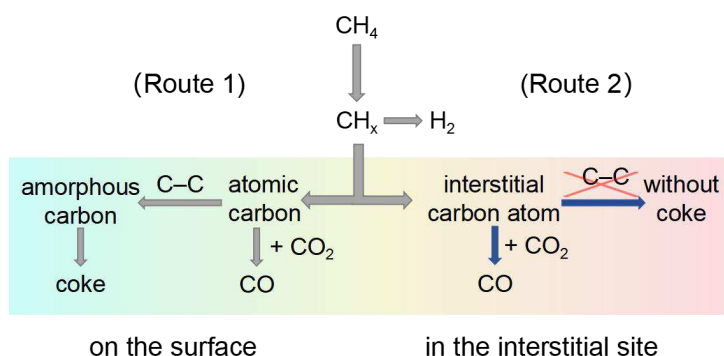
26 atoms can be replenished and cycled in Ni₃ZnC_{0.7} interior structure rather than
27 depositing as coke on the surface during the reaction as revealed by in situ
28 experiments.

29 **Introduction**

30 Two kinds of most abundant greenhouse gas, CH₄ and CO₂, originated from biogas,
31 natural or shale gas, landfill gas, off-gas (coke oven gas, blast furnace gas) and purge
32 gas, can be utilized through an endothermic reforming reaction (dry reforming of
33 methane, $\text{CO}_2 + \text{CH}_4 \rightleftharpoons 2\text{CO} + 2\text{H}_2$) to produce synthesis gas (syngas, CO and H₂) as
34 an essential building block for liquid fuels and chemicals [1-5]. Therefore, dry
35 reforming of methane (DRM) has attracted tremendous interests and attentions in
36 environment and energy implications from the aspects of designing and developing
37 robust Ni-based catalysts with high catalytic-performance. However, the coke
38 deposition on Ni particles is the main origin for the pervasive deactivation of catalyst
39 [6-9].

40 According to previous literature, CH₄ first dissociates into carbon atom on the
41 surface of Ni particles, as illustrated in Fig. 1 (Route 1) [10-12]. These carbon atoms are
42 highly active and can be converted to CO when reacting with CO₂ through $\text{CO}_2 + \text{C} \rightleftharpoons$
43 2CO . In addition, the polymerization of carbon atoms by C-C bond formation
44 generates unwanted amorphous carbon species, which can further grow and
45 crystallize to coke deposition. It is therefore desirable and essential to restrain the
46 formation of coke by promoting CO₂ activation for quick carbon gasification or by
47 preventing CH₄ dissociation for slow carbon deposition [13, 14]. In general, carbon
48 atoms can locate on the surface or inside the Ni particles [15-17]. If these atoms are
49 incorporated into the interstitial position in the nickel octahedral sites (O-sites), owing
50 to their larger free volume (or radius of O-sites) in comparison with the tetrahedral

51 sites, these carbon atoms will be isolated and the formation of coke is prohibited in
 52 principle, which is denoted as Route 2 in Fig. 1.



53

54 **Fig. 1: Schematic illustration of the proposed process.** The evolution of carbon
 55 species on the surface (Route 1, with the presence of coke deposition) and in the
 56 interstitial site (Route 2, without coke formation) of Ni during DRM reaction.

57 However, the space volume of O-site in face-centered cubic nickel is not able to
 58 accommodate carbon atoms, instead these atoms would dissolution on surface to
 59 accumulate as coke deposition by Route 1 [18, 19]. It should be noted that the
 60 introduction of second metal, for instance Zn, to Ni could effectively expand the
 61 lattice parameters, which provides the chance and feasibility for the diffusion of
 62 carbon atoms to O-sites. Recently, oxidized carbon nanotube (oCNT) supported Ni_3Zn
 63 was developed to manipulate interstitial carbon atoms into the O-site with the
 64 formation of interstitial $\text{Ni}_3\text{ZnC}_{0.7}/\text{oCNT}$. The transformation from Ni_3Zn to $\text{Ni}_3\text{ZnC}_{0.7}$
 65 on oCNT was achieved under 1.0 vol% $\text{C}_2\text{H}_2/\text{H}_2$, contributing to an enhanced
 66 selectivity and stability for the hydrogenation of alkyne [20]. However, it has been
 67 reported that the incorporation of carbon atoms in the O-site of nickel on industrially
 68 used Al_2O_3 support is still a big challenging task.

69 Described here, we present a reaction-induced method to obtain Al_2O_3 encapsulated
 70 $\text{Ni}_3\text{ZnC}_{0.7}$ ($\text{Ni}_3\text{ZnC}_{0.7}/\text{Al}_2\text{O}_3$) with superstructure feature under CH_4/CO_2 atmosphere
 71 from $\text{Ni}_3\text{Zn}/\text{Al}_2\text{O}_3$. We first synthesized the ZIF-8/Ni-Al layered double hydroxide

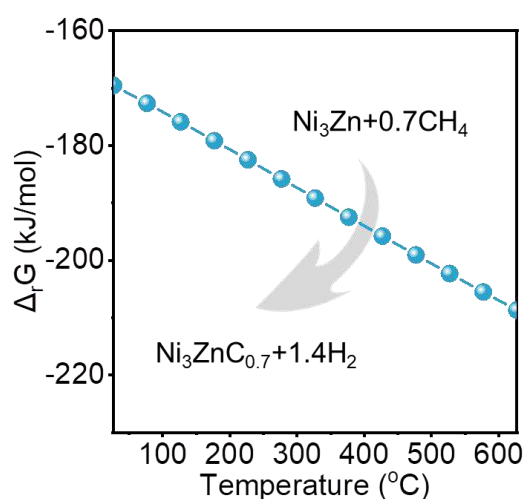
72 (Ni–Al LDH) composite by a two-step method, which was then calcinated under air
73 and further reduced under H₂ to form Ni₃Zn/Al₂O₃. The carbon atoms from CH₄
74 disassociation, as illustrated in Fig. 1, were incorporated into the interstitial O-site of
75 Ni₃Zn structure, and these atoms in superstructure Ni₃ZnC_{0.7} were cycled (Route 2)
76 during the DRM, where the incorporated carbon atoms can be converted by CO₂.

77 **Results**

78 **Reaction-induced process for the generation of Ni₃ZnC_{0.7}/Al₂O₃.** In this work,
79 ZIF-8/NiAl–LDH composite was obtained by a two-step procedure, including the first
80 synthesis of ZIF-8 at room temperature and the subsequent growth of NiAl–LDH on
81 ZIF-8 by hydrothermal method. This is confirmed by the presence of diffraction peaks
82 of ZIF-8 and NiAl–LDH on the composite (Supplementary Fig. 1 a, b). Meanwhile,
83 the cubic ZIF-8 covered by sheet-like NiAl–LDH was observed on the composite
84 (Supplementary Fig. 1 c, d). Further calcination of the ZIF-8/NiAl–LDH at 500°C
85 under air led to the formation of NiO–ZnO/Al₂O₃, which has a surface area of 120 m²
86 g⁻¹. Ni, Zn, and Al contents on the sample were 40.4 wt%, 22.6 wt%, and 5.7 wt%,
87 respectively, as determined by inductively coupled-plasma atomic emission
88 spectroscopy (ICP–AES) measurement. X-ray diffraction (XRD) pattern of
89 NiO–ZnO/Al₂O₃ showed obvious diffraction peaks for NiO and ZnO, whereas the
90 absence of the peaks for Al₂O₃ indicates the presence of amorphous structure
91 (Supplementary Fig. 2). Furthermore, ZnO particles (red color for Zn element) were
92 closely interacted with NiO (blue color for Ni element) and Al₂O₃ (orange color for Al
93 element) (Supplementary Fig. 3). Besides, Ni and Al species were homogeneously
94 dispersed on the resultant layered double oxide with nanosheets morphology.

95 The reaction-induced process for the formation of Ni₃ZnC_{0.7}/Al₂O₃ is illustrated in
96 Supplementary Fig. 4, including H₂ reduction and subsequent DRM. NiO–ZnO/Al₂O₃

97 was first reduced to $\text{Ni}_3\text{Zn}/\text{Al}_2\text{O}_3$ under H_2 reduction, and then transferred to
98 $\text{Ni}_3\text{ZnC}_{0.7}/\text{Al}_2\text{O}_3$ upon switching to the feedstock gases of CH_4 and CO_2 , which was
99 originated from the incorporation of carbon atoms into O-sites of Ni_3Zn . In addition,
100 the origin of carbon atom in $\text{Ni}_3\text{ZnC}_{0.7}$ during DRM was verified through
101 temperature-programmed surface reaction (TPSR) experiments under CH_4 or CO
102 condition, separately. The presence of H_2 from CH_4 dissociation at around 298°C
103 rather than the formation of CO_2 from CO disproportionation reveals that the
104 interstitial carbon atoms come from CH_4 dissociation (Supplementary Fig. 5). Fig. 2
105 shows the calculated Gibbs free energy change (Δ_rG) of the reaction between Ni_3Zn
106 and CH_4 in following equation: $\text{Ni}_3\text{Zn} + 0.7\text{CH}_4 \rightarrow \text{Ni}_3\text{ZnC}_{0.7} + 1.4\text{H}_2$ (Equation 1).
107 Generally, DRM and CH_4 disassociation thermodynamically prefers to occur at the
108 temperature above 645 and 557°C , respectively [21, 22]. Notably, the reaction (Equation
109 1) is favorable at the temperature below 600°C with a highly negative Δ_rG , which is
110 indicative of the spontaneous formation of $\text{Ni}_3\text{ZnC}_{0.7}$ from the reaction between Ni_3Zn
111 and CH_4 .



112

113 **Fig. 2: Thermodynamic study.** The blue line represents the calculated Gibbs free
114 energy change (Δ_rG) for the formation of $\text{Ni}_3\text{ZnC}_{0.7}$ and H_2 from the reaction between
115 Ni_3Zn and CH_4 .

116 **Catalytic evaluation of Ni₃ZnCo_{0.7}/Al₂O₃ with different CH₄/CO₂ ratio.** Catalytic
117 performance of Ni₃ZnCo_{0.7}/Al₂O₃ during DRM was evaluated with different CH₄/CO₂
118 ratio from 1/4 to 4/1 below 600°C (Fig. 3a–c). For CH₄/CO₂ = 1/1, CH₄ and CO₂
119 conversions increased from 7.1% and 12.3% at 450°C to 39.6% and 52.6% at 600°C
120 (Fig. 3a, b), separately, accompanied by the improved H₂/CO ratio from 0.45 at 450°C
121 to 0.72 at 600°C, respectively (Fig. 3c). By dropping the CO₂ partial pressure in the
122 feedstock gases, for example, changing CH₄/CO₂ ratio to 2/1, the CH₄ conversion
123 dropped to 29.3%, whereas the CO₂ conversion increased to 67.6% at 600°C. Further
124 increasing CH₄/CO₂ ratio to 4/1, CH₄ and CO₂ conversions reached 21.1% and 81.9%
125 at 600°C, respectively. Notably, H₂/CO ratio increased progressively with the highest
126 value of 0.96 at 600°C when CH₄ partial pressure increased in the feed gas.

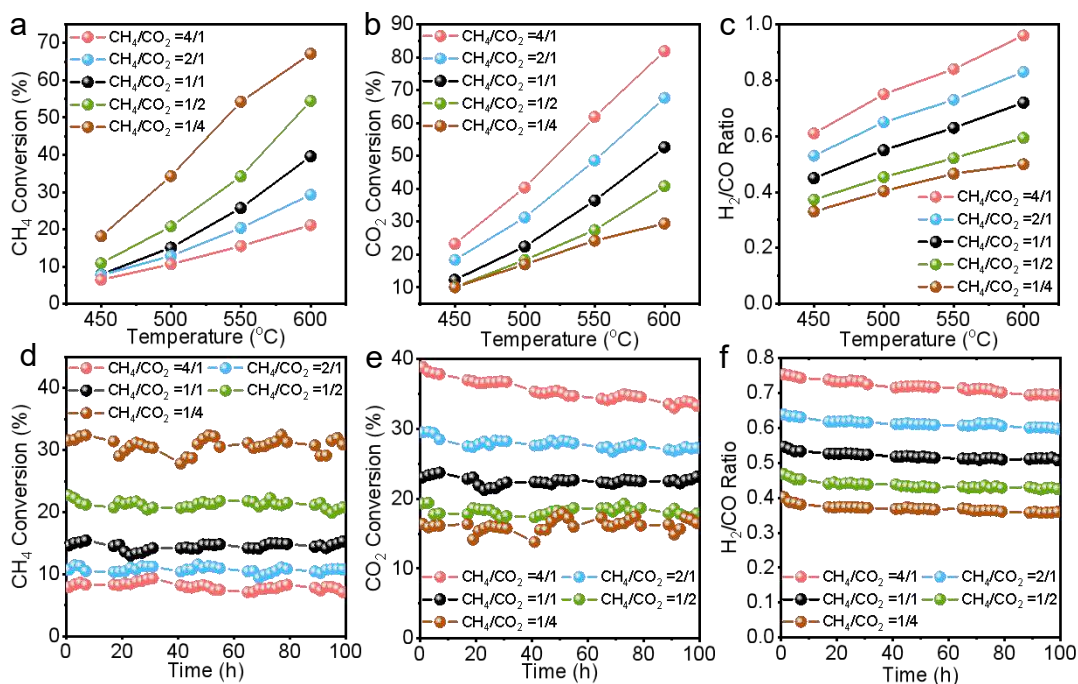
127 The increase of CO₂ partial pressure in the feedstock indeed improved the CH₄
128 conversion, as consistent with the results of increase of CH₄ partial pressure in the
129 feedstock gases for CO₂ conversion. CH₄ conversion ranged from 10.9% at 450°C to
130 54.5% at 600°C with the CH₄/CO₂ ratio of 1/2, which further increased from 18.2% at
131 450°C to 67.1% at 600°C with the CH₄/CO₂ ratio of 1/4. CO₂ conversion declined
132 with the CH₄/CO₂ ratio decreasing from 1/2 to 1/4, such as from 40.7% to 29.5% at
133 600°C. Compared to CH₄/CO₂ ratio of 1/2, H₂/CO ratio decreased apparently with the
134 ratio of 1/4 at the same temperature. It should be noted that the maximum CH₄ or CO₂
135 conversion of 67.1% or 81.9% at 600°C is much higher than the equilibrium value
136 under the stoichiometric reaction, when CH₄ or CO₂ partial pressure in the feedstock
137 was varied.

138 The catalytic stability of Ni₃ZnCo_{0.7}/Al₂O₃ was investigated at 500°C for a 100 h
139 period, as illustrated in Fig. 3d–f. The catalyst showed a high stability of CH₄ and
140 CO₂ conversion, regardless of CH₄/CO₂ ratio of 1/1 and 2/1, which is stabilized

141 around 15% and 23% under the ratio of 1/1 and 11% and 27% under the ratio of 2/1,
142 respectively (Fig. 3d, e). The H₂/CO ratio was relatively stable at around 0.51 (the
143 ratio of 1/1) and 0.61 (the ratio of 2/1), except for the slightly decline in the initial
144 period (Fig. 3f). However, for CH₄/CO₂ ratio of 4/1, CH₄ and CO₂ conversion
145 decreased from 8% to 7% and 38% to 33%, separately, and H₂/CO ratio dropped from
146 0.75 to 0.69. Thus, it is indicated that a higher CH₄/CO₂ ratio of 4/1 played a
147 detrimental effect on the catalytic performance for Ni₃ZnCo_{0.7}/Al₂O₃ in DRM.
148 Ni₃ZnCo_{0.7}/Al₂O₃ also exhibited stable values of CH₄ and CO₂ conversion during the
149 long-term stability test in low CH₄/CO₂ ratio, being around 22% and 18% under the
150 ratio of 1/2 and 32% and 17% under the ratio of 1/4, respectively. H₂/CO ratio
151 declined in the first 9 h and maintained at 0.36 and 0.43 for the ratio of 1/2 and 1/4,
152 respectively.

153 Considering the feedstock source of CO₂ and CH₄, the composition of the mixture
154 could be tailored and formulized on the basis of alternative CH₄/CO₂ ratio [2, 23, 24].
155 However, a high CH₄/CO₂ ratio is prone to produce carbonaceous deposition, and a
156 low CH₄/CO₂ ratio provides oxidation environment relative to the reactive centre,
157 leading to the presence of NiO shells covering Ni particles. Meanwhile, DRM
158 requires high temperature (800–900°C) to achieve the CH₄ conversion higher than
159 50% [10, 25]. Notably, the robust Ni₃ZnCo_{0.7}/Al₂O₃ possesses 67.1% of CH₄ conversion
160 under CH₄/CO₂=1/4 at 600°C and is stable for the long-term test. A differential reactor
161 for Ni₃ZnCo_{0.7}/Al₂O₃ was then used to measure reaction order and activation energy.
162 The kinetic parameters were achieved independently of CH₄ or CO₂ partial pressure
163 on Ni₃ZnCo_{0.7}/Al₂O₃ during the reaction (Supplementary Fig. 6 and Supplementary
164 Table 2, 3). The reaction orders of CH₄ and CO₂ were 1.37 and 1.57, respectively. The
165 measured activation energies of CO₂ and CH₄ were 52 ± 4 kJ mol⁻¹ and 112 ± 4 kJ

166 mol⁻¹, respectively.

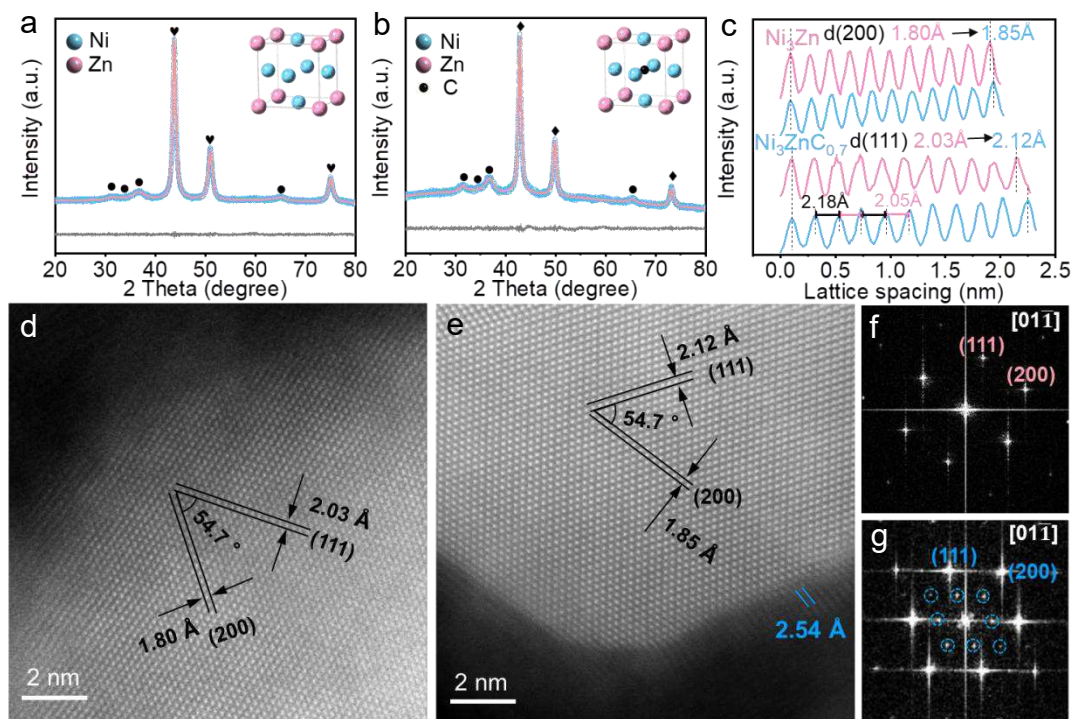


167

168 **Fig. 3: Catalytic evaluation of Ni₃ZnC_{0.7}/Al₂O₃.** (a) CH₄, (b) CO₂ conversion, and (c)
 169 H₂/CO ratio of Ni₃ZnC_{0.7}/Al₂O₃ for DRM under different CH₄/CO₂ ratio between 450
 170 and 600°C. (d) CH₄, (e) CO₂ conversion, and (f) H₂/CO ratio of Ni₃ZnC_{0.7}/Al₂O₃ for
 171 DRM under different CH₄/CO₂ ratio at 500°C for 100 h.

172 **Characterizations of Ni₃Zn/Al₂O₃ and Ni₃ZnC_{0.7}/Al₂O₃.** The crystal structures of
 173 Ni₃Zn/Al₂O₃ after H₂ reduction and Ni₃ZnC_{0.7}/Al₂O₃ after stoichiometric reaction with
 174 100 h period were determined by Rietveld refinement of XRD, as shown in Fig. 4a
 175 and b. In addition to the peaks for ZnO on both samples, the reduced catalyst
 176 presented the peaks characterized for face-centered cubic Ni₃Zn; however, for
 177 Ni₃ZnC_{0.7}/Al₂O₃, the peaks shifted to smaller 2θ values, which suggests a larger unit
 178 cell, originating from the incorporation of interstitial carbon atoms into the O-sites of
 179 Ni₃Zn. Notably, the evolution from Ni₃Zn to Ni₃ZnC_{0.7} occurred regardless of
 180 feedstock gas ratio for the non-stoichiometric or stoichiometric reaction as evidenced
 181 by the larger unit cell of Ni₃ZnC_{0.7} in comparison with that of Ni₃Zn from the Rietveld

182 refinement (Supplementary Fig. 7 and Table 1). It is worth noting that compared with
 183 the catalysts after 100 h run with the CH₄/CO₂ ratio larger than 1/1, small portion of
 184 Ni₃Zn and ZnO were present when the ratio is less than 1/1.



185
 186 **Fig. 4: Characterizations of Ni₃Zn/Al₂O₃ and Ni₃ZnC_{0.7}/Al₂O₃.** a, b, Refined XRD
 187 patterns and crystal structures of (a) Ni₃Zn/Al₂O₃ and (b) Ni₃ZnC_{0.7}/Al₂O₃. ●, ♥, and
 188 ♦: ZnO, Ni₃Zn, and Ni₃ZnC_{0.7}. c, Inter-planar spacing of (111) and (200) from STEM
 189 images of Ni₃Zn/Al₂O₃ and Ni₃ZnC_{0.7}/Al₂O₃. d–g, Atomic-resolution HAADF-STEM
 190 images with FFT images of (d, f) Ni₃Zn/Al₂O₃ and (e, g) Ni₃ZnC_{0.7}/Al₂O₃.

191 High angle annular dark field-scanning transmission electron microscopy
 192 (HAADF-STEM) was employed to investigate the atomic structures of Ni₃Zn and
 193 Ni₃ZnC_{0.7}, as shown in Fig. 4d and e. Clearly, the well-defined (111) and (200) lattice
 194 planes with the acute angle of 54.7° were observed on Ni₃Zn (Fig. 4d) and Ni₃ZnC_{0.7}
 195 (Fig. 4e), and the edge of Ni₃ZnC_{0.7}/Al₂O₃ exhibited the lattice space of 2.54 Å,
 196 indicating the presence of Al₂O₃ (020). Average inter-distances of (111) and (200)
 197 planes further revealed the lattice expansion of Ni₃ZnC_{0.7} deriving from the

198 incorporation of carbon atoms into Ni₃Zn (Fig. 4c). The corresponding fast Fourier
 199 transform (FFT) image of Ni₃Zn indicate its single crystalline character (Fig. 4f), and
 200 the incorporated carbon atoms induced a superstructure feature of formed Ni₃ZnC_{0.7},
 201 which was verified by the satellite spots (highlighted in dotted circles) of its FFT
 202 image in Fig. 4g.

203 **Table 1.** The structure, cell parameters and carbon formation rate of the reduced
 204 Ni₃Zn/Al₂O₃ and Ni₃ZnC_{0.7}/Al₂O₃ after 100 h reaction under different CH₄/CO₂ ratio.

Condition ^a	Structure ^b			Cell parameters	R _{wp}	R _c
	Ni ₃ Zn	Ni ₃ ZnC _{0.7}	ZnO	a=b=c (Å)	(%) ^c	(mg _c g _{cat} ⁻¹ h ⁻¹) ^d
H ₂	95.48%	N.A.	4.52%	3.5066641	1.78	N.A.
R=4/1	N.A.	95.45%	2.41%	3.6582036	2.64	3.17
R=2/1	N.A.	97.12%	2.84%	3.6575336	2.79	0.445
R=1/1	N.A.	98.75%	1.25%	3.6597136	2.97	0.376
R=1/2	3.58%	87.15%	9.27%	3.6385673	2.63	0.266
R=1/4	4.74%	88.16%	7.07%	3.5265675	2.75	0.232

205 ^a represents H₂ reduction and variable CH₄/CO₂ (R) ratio. ^b refers to the
 206 composition component of the catalysts after H₂ reduction and 100 h reaction from
 207 refinement of XRD. The catalyst after 100 h period with R=4/1 contains extra 2.13%
 208 carbon. ^c refers to the weighted profile factor of the Rietveld refinement of XRD. ^d
 209 represents the carbon deposition rate calculating from the following equation: R_c =
 210 $\frac{m_c}{m_{cat} \cdot 100 \text{ h}}$, where m_c and m_{cat} represent the amount of carbon on the spent catalyst and
 211 the mass of catalyst, respectively.

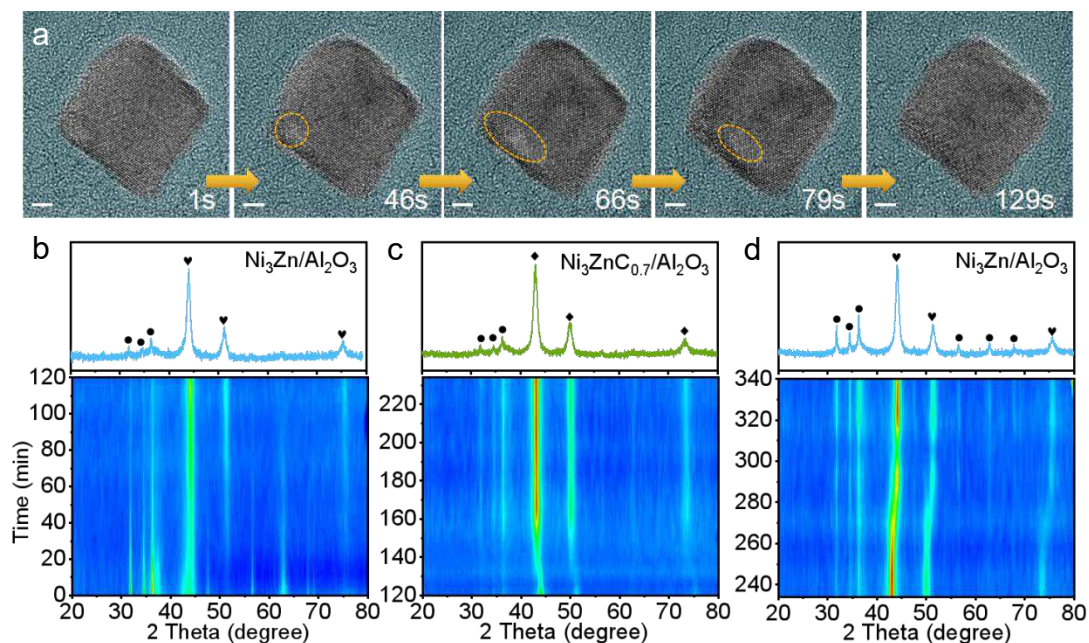
212 A couple of shorter and longer distance in the example of (111) inter-planar spacing
 213 was measured, which further verified the presence of the superstructure feature (Fig.
 214 4c). This could probably result from the incorporation of carbon atoms. The

215 superstructure spots also existed on different particle with different crystal axis
216 directions as shown in Supplementary Fig. 8. Furthermore, $\text{Ni}_3\text{ZnC}_{0.7}/\text{Al}_2\text{O}_3$ particle
217 exhibited a core-shell structure with inner $\text{Ni}_3\text{ZnC}_{0.7}$ encapsulated by the thin-layer
218 Al_2O_3 of about 2 nm. This was confirmed by the presence of lattice space of 2.12 Å
219 for $\text{Ni}_3\text{ZnC}_{0.7}$ (111) and 2.54 Å for Al_2O_3 (020) with low crystalline at the interface
220 and amorphous form on the outer shell, respectively (Fig. 4e and Supplementary Fig.
221 9).

222 **Cycles of carbon atoms in $\text{Ni}_3\text{ZnC}_{0.7}$ for DRM.** In situ environmental transmission
223 electron microscopy (ETEM) measurement was performed to investigate the dynamic
224 process of structure changes during DRM (Fig. 5a). The reduced $\text{Ni}_3\text{Zn}/\text{Al}_2\text{O}_3$ was
225 obtained by ex situ reduction under H_2 at 550°C for 2 h, and then stored in Ar
226 atmosphere before loading into ETEM. The reduced $\text{Ni}_3\text{Zn}/\text{Al}_2\text{O}_3$ sample was firstly
227 heated to 500°C and then exposed to the CH_4/CO_2 (1/1) stream. The time-dependent
228 change of individual particle was recorded by high-resolution TEM (HRTEM)
229 measurement. The lattice variation of Ni_3Zn particle occurred near its surface and
230 gradually expanded, which could be attributed to the penetration of carbon source
231 (atoms), as highlighted in Fig. 5a and indicated in color-coded images
232 (Supplementary Fig. 10a and Movie 1). The varied region was decreased and
233 eventually formed the $\text{Ni}_3\text{ZnC}_{0.7}$ phase which was confirmed by the corresponding
234 fast FFT image with satellite points (Supplementary Fig. 10b).

235 In situ electron energy-loss spectroscopy (EELS) measurement was further
236 conducted to verify the incorporation of carbon atom into Ni_3Zn (Supplementary Fig.
237 11). The EELS spectrum of $\text{Ni}_3\text{Zn}/\text{Al}_2\text{O}_3$ showed no carbon signal at room
238 temperature without introducing feedstock gases, whereas the carbon K-edge EELS
239 presented an apparent peak around 294 eV under CH_4/CO_2 (1/1) stream at 500°C.

240 This carbon signal still remained after removing the reactants and even cooled down
241 to room temperature, which suggests the stable structure of the carbon-incorporated
242 $\text{Ni}_3\text{ZnC}_{0.7}/\text{Al}_2\text{O}_3$.



243

244 **Fig. 5: In situ studies of the cycles of carbon atoms.** **a**, In situ HRTEM images on
245 the evolution from Ni_3Zn to $\text{Ni}_3\text{ZnC}_{0.7}$ under the stoichiometric reaction at 500°C .
246 Scale bar: 2 nm. **b**, **c**, **d**, Time-resolved in situ XRD patterns of the evolution of **(b)**
247 $\text{NiO-ZnO}/\text{Al}_2\text{O}_3$ to $\text{Ni}_3\text{Zn}/\text{Al}_2\text{O}_3$ under H_2 at 550°C , **(c)** further to $\text{Ni}_3\text{ZnC}_{0.7}/\text{Al}_2\text{O}_3$
248 under $\text{CH}_4/\text{CO}_2=1/1$ at 500°C , and **(d)** back to $\text{Ni}_3\text{Zn}/\text{Al}_2\text{O}_3$ by CO_2 treatment at
249 500°C . ●, ♥ and ◆: ZnO , Ni_3Zn and $\text{Ni}_3\text{ZnC}_{0.7}$.

250 Since the incorporated carbon atoms in $\text{Ni}_3\text{ZnC}_{0.7}/\text{Al}_2\text{O}_3$ were originated from CH_4
251 dissociation, the structures of carbon species in $\text{Ni}_3\text{ZnC}_{0.7}/\text{Al}_2\text{O}_3$ (after 100 h reaction)
252 with different CH_4/CO_2 ratio were investigated by Raman characterization. In addition
253 to the peaks for Ni-C and Zn-C vibration modes at 508 cm^{-1} on the Raman spectra of
254 $\text{Ni}_3\text{ZnC}_{0.7}/\text{Al}_2\text{O}_3$ [26, 27], the characteristic bands for extra carbon deposition (D and G
255 bands at 1338 and 1578 cm^{-1}) were observed and became predominant with
256 enhancement of the CH_4/CO_2 ratio to 4/1 (Supplementary Fig. 12). However, the

257 presence of Ni–C and Zn–C bands without formation of carbonaceous species was
258 only detected under the condition of $\text{CH}_4/\text{CO}_2 < 1/1$.

259 The carbon deposition rates on $\text{Ni}_3\text{ZnC}_{0.7}/\text{Al}_2\text{O}_3$ after 100 h reaction with different
260 CH_4/CO_2 ratio are shown in Table 1. The theoretical carbon formation rate of
261 $\text{Ni}_3\text{ZnC}_{0.7}$ from Ni_3Zn is $0.373 \text{ mg}_c \text{ g}_{\text{cat}}^{-1} \text{ h}^{-1}$ after 100 h period. The carbon deposition
262 rate is lower than theoretical value with CH_4/CO_2 ratio less than 1/1, which indicates
263 the formation of non-stoichiometric $\text{Ni}_3\text{ZnC}_{0.7}$ with carbon vacancies. However, large
264 carbon deposition rate is observed on $\text{Ni}_3\text{ZnC}_{0.7}/\text{Al}_2\text{O}_3$ after reaction when CH_4/CO_2
265 ratio was higher than 1/1. The highest carbon deposition rate of $3.17 \text{ mg}_c \text{ g}_{\text{cat}}^{-1} \text{ h}^{-1}$ was
266 obtained on $\text{Ni}_3\text{ZnC}_{0.7}/\text{Al}_2\text{O}_3$ after stability test under $\text{CH}_4/\text{CO}_2 = 4/1$, leading to the
267 deactivation of catalytic properties. Meanwhile, large amounts of inactive coke
268 (carbon filaments) were formed on the spent $\text{Ni}_3\text{ZnC}_{0.7}/\text{Al}_2\text{O}_3$ with the ratio up to 4/1.
269 This is the main origin for the decline of the long-term stability in Fig. 3 (deposited
270 carbon species from Route 1 in Fig. 1). The scanning electron microscopy (SEM) and
271 TEM images further indicated that no coke species were formed on the spent catalysts
272 after 100 h reaction when CH_4/CO_2 ratio was less than 4/1 (Supplementary Fig. 13
273 and Supplementary Fig. 14).

274 The incorporation and extraction cycles of carbon atoms between Ni_3Zn and
275 $\text{Ni}_3\text{ZnC}_{0.7}$ under steady-state DRM reaction and under subsequent CO_2 treatment were
276 studied through time-resolved in situ XRD measurement, as shown in Fig. 5b–c and
277 Supplementary Fig. 15. The intensity of peaks for ZnO and NiO decreased gradually,
278 which was accompanied by the presence of the peaks for Ni_3Zn under H_2 reduction at
279 550°C (Fig. 5b). Once the catalyst was exposed to the reactants ($\text{CH}_4/\text{CO}_2 = 1/1$) at
280 500°C , the peaks of Ni_3Zn (111) and (200) declined, whereas the peaks of $\text{Ni}_3\text{ZnC}_{0.7}$
281 (111) and (200) appeared when reacting for 18 min and being stabilized with reaction

282 for 42 min (Fig. 5c). This confirms the incorporation of carbon atoms into O-sites in
283 Ni₃Zn to form Ni₃ZnC_{0.7}. After the reaction, CO₂ was switched into the reaction cell.
284 The extraction of carbon atom in Ni₃ZnC_{0.7} occurred as evidenced by the reversible
285 transfer to Ni₃Zn by the Boudouard reaction (Fig. 5d). Carbon atoms in Ni₃ZnC_{0.7} is
286 able to be donated and replenished when reacting with CO₂ and CH₄, respectively. We
287 further conducted the pulse experiment of CH₄-Ar-CO₂-Ar-CH₄ to demonstrate the
288 cycles of carbon atoms (Supplementary Fig.16). The stable performance indicates the
289 reversible transfer of carbon atoms between Ni₃ZnC_{0.7} and Ni₃Zn. It is therefore noted
290 that carbon cycles exist during DRM, including carbon atom incorporating into
291 Ni₃ZnC_{0.7} as active carbon reservoir, and then consumed by CO₂ to recover the Ni₃Zn
292 structure (Supplementary Fig. 17).

293 **Conclusion**

294 In the present work, we propose a method to sink the surface carbon atoms into the
295 interstitial sites of Ni₃Zn to form Ni₃ZnC_{0.7} during DRM with different feedstock ratio.
296 Carbon atoms on Ni surface are preferred to polymerize and accumulate as the
297 deactivated coke deposition (Route 1, in Fig. 1), whereas these atoms in the nickel
298 octahedral sites are isolated in the highly active nature, inhibiting the presence of
299 undesirable carbonaceous species especially under CH₄/CO₂ < 1/1 (Route 2, in Fig. 1).
300 Interstitial carbon atoms in Al₂O₃ encapsulated Ni₃ZnC_{0.7} with superstructure feature
301 can be developed under reaction-induced conditions, contributing to the enhanced
302 catalytic activity and stability at temperature below 600°C under either stoichiometric
303 or non-stoichiometric (CH₄/CO₂ < 4/1) condition. The dynamic properties of
304 interstitial carbon atoms are systematically characterized and discussed by in situ
305 TEM, EELS and XRD measurements in details. The carbon atoms in Ni₃ZnC_{0.7} are
306 cycled during the reaction, where these occupied atoms can be consumed by CO₂

307 through the Boudouard reaction and restored by CH₄ through its dissociation. The
308 present idea for the control of interstitial carbon atoms can be extended to
309 incorporating other atoms, which shall further pave the way for other reforming
310 reactions, such as steam reforming and partial oxidation as well as selective
311 hydrogenation reactions [28, 29].

312 **Methods**

313 **Synthesis of ZIF-8.** Metal-organic framework, ZIF-8 as ZnO precursor, was prepared
314 by a facile method based on the previous literature [30]. Typically, 0.1 M aqueous
315 solution of zinc acetate (5 mL) was dropwisely added into 9.5 mL ammonia solution
316 (25%–28%) dissolved with 2-methylimidazole (0.675 g), and vigorous stirring at
317 room temperature for 4 h. The white product was collected by centrifugation under
318 the rotation speed of 4500 r min⁻¹ and washed with deionized water. This process was
319 repeated for three times and dried at 80°C for 12 h.

320 **Growth of ZIF-8/Ni–Al layered double hydroxide (LDH) composite.** First,
321 as-prepared ZIF-8 (2.0 g) was dissolved into 50 mL of Na₂CO₃ solution (0.75 M)
322 under gentle stirring for 1 h to form a turbid solution. Subsequently, a mixture
323 solution (1.876 g of Al(NO₃)₃·9H₂O and 4.362 g of Ni(NO₃)₂·6H₂O in 20 mL of
324 deionized water) together with NaOH solution (1.5 M) were added into the above
325 turbid solution stepwise under vigorous stirring to maintain the whole pH value of 11.
326 The solution was then transferred and sealed into 100 mL Teflon-lined stainless steels
327 and placed in an oven for 24 h at 120°C. Finally, the ZIF-8/Ni–Al LDH composite
328 was collected by centrifugation (rotation speed of 4500 r min⁻¹), and washed with
329 deionized water until reaching the neutral pH value, and finally dried at 80°C under
330 vacuum for 12 h.

331 **Formation of Ni₃Zn/Al₂O₃ by H₂ reduction.** The ZIF-8/Ni–Al LDH composite was

332 calcinated at 500°C for 3 h with a heating rate of 2°C min⁻¹ under air. The resultant
333 celadon sample is denoted as NiO–ZnO/Al₂O₃. NiO–ZnO/Al₂O₃ was then reduced at
334 550°C under H₂ (20 mL min⁻¹) for 2 h to form Ni₃Zn/Al₂O₃ (black solid powder).

335 **Reaction-induced synthesis of Ni₃ZnC_{0.7}/Al₂O₃ catalyst.** The reduced Ni₃Zn/Al₂O₃
336 was exposed to feedstock gases of different CH₄/CO₂ ratio (from 1/4 to 4/1) during
337 DRM to form Ni₃ZnC_{0.7}/Al₂O₃ catalyst at temperature ranging from 450°C to 600°C.
338 The superstructure Ni₃ZnC_{0.7}/Al₂O₃ was produced under DRM at 500°C for 100 h.

339 **Material characterizations.** The Ni, Zn, and Al contents on NiO–ZnO/Al₂O₃ were
340 analyzed by inductively coupled-plasma atomic emission spectroscopy (ICP-AES)
341 using a Thermo iCAP 6300 spectrometer. Prior to measurement, the sample was
342 dissolved in nitric acid and then diluted with distilled water to reduce the metal ion
343 concentration below 20 ppm. The overall morphology of the samples was detected by
344 field emission scanning electron microscopy (SEM) on a JSM-7001F high-resolution
345 scanning electron microscope. The crystalline phase and component structure of the
346 samples were identified by X-ray diffraction (XRD) measurement on a Rigaku
347 SmartLab SE diffractometer (Cu K α radiation, $\lambda = 1.5418 \text{ \AA}$) at a scanning speed rate
348 of 5 ° min⁻¹. Nitrogen adsorption experiments were performed on a Quantachrome
349 NOVA 1200e analyzer at –196°C and the surface area was determined by using the
350 Brunauer–Emmett–Teller (BET) equation. Before adsorption, the sample was
351 degassed under vacuum at 300°C for 3 h to remove impurities. The carbon content in
352 Ni₃ZnC_{0.7}/Al₂O₃ after 100 h reaction was measured by elemental analysis on a vario
353 EL cube, ELEMENTAR. The structure of Ni₃ZnC_{0.7}/Al₂O₃ under different CH₄/CO₂
354 ratio was estimated by Raman spectroscopy on a DXR microscope instrument. The
355 overall morphology and structure of the catalysts were investigated by high angle
356 annular dark-field (HAADF) scanning transmission electron microscopy (STEM) on a

357 double Cs-corrected TEM (FEI Titan Themis G2) operated at 300 kV equipped with
358 Super-X EDX detector. The CH₄ or CO temperature programmed surface reaction on
359 Ni₃Zn/Al₂O₃ was carried performed on a fixed-bed reactor. One hundred milligram of
360 NiO–ZnO/Al₂O₃ (20–40 mesh) mixed with 1.0 g of quartz sand (20–40 mesh) were
361 reduced under H₂ (30 mL min⁻¹) at 550°C for 2 h, and then the temperature was
362 cooled to 35°C under Ar (30 mL min⁻¹). The signal of H₂ (m/z = 2) or CO₂ (m/z = 44)
363 was recorded on a mass spectrometer (HIDEN QGA) accompanied by the increasing
364 of temperature to 600°C with a heating rate of 10 °C min⁻¹.

365 **In Situ XRD studies.** In situ XRD patterns of NiO–ZnO/Al₂O₃ during H₂ reduction
366 and DRM were obtained on a Rigaku SmartLab SE diffractometer (Cu K α radiation).
367 The NiO–ZnO/Al₂O₃ was loaded in reaction cell and the temperature was increased to
368 550°C with a heating rate of 10°C min⁻¹ under Ar. Afterwards, H₂ (20 mL min⁻¹) was
369 introduced into the reaction cell for the reduction process. The XRD patterns were
370 recorded with a scanning rate of 10 ° min⁻¹. Next, the cell was cooled down to 500°C.
371 CH₄ (20 mL min⁻¹) and CO₂ (20 mL min⁻¹) were switched into the cell, and the XRD
372 data were collected with the same scanning speed. To study the reactivity of carbon
373 atoms in Ni₃ZnC_{0.7}/Al₂O₃ with CO₂, the aforementioned sample in the cell was
374 exposed to CO₂ (20 mL min⁻¹) at 500°C, and the XRD data were collected with the
375 same scanning speed.

376 **Environmental transmission electron microscopy (ETEM) experiment.** The in
377 situ transmission electron microscopy (TEM) study was conducted on an
378 image-aberration-corrected FEI Titan G2 80-300 ETEM operated at 300 kV. The
379 specimen was loaded onto a chip of the MEMS (microelectromechanical
380 systems)-based heating holder (FEI Nano-Ex). The reduced Ni₃Zn/Al₂O₃ was first
381 heated to 500°C with a rate of 10°C s⁻¹ and stabilized for 20 min under high vacuum

382 ($\sim 10^{-5}$ Pa) with the e-beam off. Afterwards, the $\text{CH}_4/\text{CO}_2 = 1/1$ stream was introduced
383 and reached to a pressure of ~ 0.8 mbar. TEM images and video were recorded at a
384 dose rate of $\sim 1000 \text{ e } \text{\AA}^{-2} \text{ s}^{-1}$ under an exposure time of 0.25 s (each 4 frames combined
385 into one image and each image was 1 s). In situ scanning transmission electron
386 microscopy–electron energy-loss spectroscopy (STEM–EELS) data were collected by
387 a Gatan image filter (Quantum 936) with an energy dispersion of 0.5 eV. The
388 zero-loss EELS was also acquired for the background subtraction of corresponding
389 core-loss EELS. The analysis of obtained TEM data was performed on
390 DigitalMicrograph (version 2.33) and ImageJ (version 1.52a).

391 **Catalytic evaluation of dry reforming of methane.** DRM was carried out in a
392 fixed-bed reactor under atmospheric pressure. For the catalytic investigations, 0.1 g of
393 $\text{NiO–ZnO/Al}_2\text{O}_3$ (20–40 mesh) mixed with 1.0 g of quartz sand (20–40 mesh) were
394 loaded into a quartz tube (internal diameter of 8 mm and length of 450 mm). The
395 sample was first heated to 550°C in Ar (30 mL min^{-1}) with a rate of $10^\circ\text{C min}^{-1}$ and
396 reduced with H_2 (30 mL min^{-1}) for 2 h. Next, the sample was cooled down to 450°C in
397 Ar. The DRM was performed at the temperature of 450, 500, 550 and 600°C (each
398 temperature for 1 h) in CH_4 and CO_2 with different CH_4/CO_2 ratio. The feedstock gas
399 ratio of CH_4/CO_2 was changed from 1/4 to 4/1 with a total amount 30 mL min^{-1} . The
400 gas hourly space velocity (GHSV) of reactant was controlled to $18,000 \text{ mL g}^{-1} \text{ h}^{-1}$. For
401 the stability evaluation, the procedure was the same as the activity test except for the
402 reaction temperature being kept at 500°C for 100 h under different CH_4 to CO_2 ratio.
403 The amounts of CH_4 , CO_2 , CO and H_2 produced were determined using an online gas
404 chromatograph (Agilent 7820A) equipped with a thermal conductivity detector
405 (TCD).

406 The CH_4 and CO_2 conversions as well as H_2/CO ratio were calculated using the

407 following formula:

$$408 \quad \text{CH}_4 \text{ conversion (\%)} = \frac{(F_{\text{CH}_4,\text{in}} - F_{\text{CH}_4,\text{out}})}{F_{\text{CH}_4,\text{in}}} \times 100\%$$

$$409 \quad \text{CO}_2 \text{ conversion (\%)} = \frac{(F_{\text{CO}_2,\text{in}} - F_{\text{CO}_2,\text{out}})}{F_{\text{CO}_2,\text{in}}} \times 100\%$$

$$410 \quad \text{H}_2/\text{CO} = \frac{(F_{\text{H}_2,\text{out}})}{F_{\text{CO},\text{out}}} \times 100\%$$

411 where $F_{x,\text{in}}$ and $F_{x,\text{out}}$ represent the molar flow rate (mol s^{-1}) of component x of the
412 inlet and outlet, respectively.

413 **Kinetic Studies.** Kinetic data of $\text{Ni}_3\text{ZnC}_{0.7}/\text{Al}_2\text{O}_3$ (50 mg of catalyst with 1 g of quartz
414 sand) for DRM were obtained from CH_4 or CO_2 reaction rate, which was determined
415 by keeping partial pressure of one reactant (CH_4 or CO_2) at approximate 50 kPa and
416 varied the other pressures (CO_2 or CH_4) as about 20, 30, 40 and 50 kPa with Ar
417 balance. The reaction was conducted at the temperatures of 390, 400, 410 and 420°C
418 to ensure the CH_4 or CO_2 conversion was maintained below 11% under differential
419 conditions. The CH_4 or CO_2 reaction rate was calculated by the following equation:

$$-r_x = \frac{F_{x,\text{in}} \cdot x_x}{m_{\text{cat}}}$$

420 where m_{cat} , $F_{x,\text{in}}$ and x_x are mass of the catalyst, molar flow rate (mol s^{-1}) and
421 conversion of the reactant (CH_4 or CO_2), respectively.

422 CH_4 reaction rate can also be expressed as the following equation:

$$r_{\text{CH}_4} = k p_{\text{CH}_4}^\alpha \times p_{\text{CO}_2}^\beta$$

423 where α and β are the reaction order of CH_4 and CO_2 , respectively, and k is the rate
424 constant. If the partial pressure of CH_4 was changed, the partial pressure of CO_2 was
425 kept constant. Therefore, we can ignore the effect of CO_2 in determining the reaction
426 order of CH_4 . The CH_4 reaction rate could be simplified as the following equation:

$$r_{\text{CH}_4} = k p_{\text{CH}_4}^\alpha + C$$

427 The reaction order of CO_2 was calculated by the same method. The activation energy

428 of CH₄ or CO₂ was achieved through the Arrhenius equation by calculating k values at
429 different temperatures.

430 **Pulse cycle test.** Pulse experiment with CH₄–Ar–CO₂–Ar–CH₄ cycles was carried
431 out in the above-mentioned fixed-bed reactor for catalytic investigation. The reaction
432 temperature for the cycle test was conducted at 600°C. After reduction, pulses of CH₄
433 (15 mL min⁻¹, 15 min, step 1) and CO₂ (15 mL min⁻¹, 15 min, step 2) were circularly
434 added to the reactor, and Ar (15 mL min⁻¹, 15 min) was used to purge the system
435 between each step. The cycles were repeated for 20 times. The evolution of the gases
436 of (CH₄, CO₂, H₂, CO) were monitored by using mass spectrometer.

437 **References**

- 438 1. Song, Y. D. et al. Dry reforming of methane by stable Ni–Mo nanocatalysts on
439 single-crystalline MgO. *Science* **367**, 777–781 (2020).
- 440 2. Angeli, S. D. et al. Reduction of CO₂ emission from off-gases of steel industry by
441 dry reforming of methane. *Angew. Chem. Int. Ed.* **60**, 11852–11857 (2021).
- 442 3. Akri, M. et al. Atomically dispersed nickel as coke-resistant active sites for
443 methane dry reforming. *Nat. Commun.* **10**, 5181 (2019).
- 444 4. Buelens, L. C., Galvita, V. V., Poelman, H., Detavernier, C. M. & Guy B.
445 Super-dry reforming of methane intensifies CO₂ utilization via Le Chatelier's
446 principle. *Science* **354**, 449–452 (2016).
- 447 5. Dong, J. H. et al. Reaction-induced strong metal-support interactions between
448 metals and inert Boron Nitride nanosheets. *J. Am. Chem. Soc.* **142**, 17167–17174
449 (2020).
- 450 6. Kim, S. M. et al. Cooperativity and dynamics increase the performance of NiFe
451 dry reforming catalysts. *J. Am. Chem. Soc.* **139**, 1937–1949 (2017).
- 452 7. Yan, X. L. et al. Highly efficient and stable Ni/CeO₂-SiO₂ catalyst for dry

453 reforming of methane: Effect of interfacial structure of Ni/CeO₂ on SiO₂. *Appl. Catal.*
454 *B: Environ.* **246**, 221–231 (2019).

455 8. Wang, J. Y. et al. Design of a carbon-resistant Ni@S-2 reforming catalyst:
456 Controllable Ni nanoparticles sandwiched in a peasecod-like structure. *Appl. Catal. B:*
457 *Environ.* **282**, 119546 (2021).

458 9. Liu, C. J., Ye, J. Y., Jiang, J. J. & Pan, Y. X. Progresses in the preparation of coke
459 resistant Ni-based catalyst for steam and CO₂ reforming of methane. *ChemCatChem*
460 **3**, 529–541 (2011).

461 10. Pakhare, D. & Spivey, J. A review of dry (CO₂) reforming of methane over noble
462 metal catalysts. *Chem. Soc. Rev.* **43**, 7813–7837 (2014).

463 11. Helveg, S. et al. Atomic-scale imaging of carbon nanofibre growth. *Nature* **427**,
464 426–429 (2004).

465 12. Trimm, D. L. Catalysts for the control of coking during steam reforming. *Catal.*
466 *Today* **49**, 3–10 (1999).

467 13. Zhang, T. T. et al. Dry reforming of methane on Ni-Fe-MgO catalysts: Influence
468 of Fe on carbon-resistant property and kinetics. *Appl. Catal. B: Environ.* **264**, 118497
469 (2019).

470 14. Nandini, A., Pant, K. K. & Dhingra, S. C. K-, CeO₂-, and Mn-promoted
471 Ni/Al₂O₃ catalysts for stable CO₂ reforming of methane. *Appl. Catal. A:Gen.* **290**,
472 166–174 (2005).

473 15. Xiao, W., Baskes, M. I. & Cho, K. MEAM study of carbon atom interaction with
474 Ni nano particle. *Surf. Sci.* **603**, 1985–1998 (2009).

475 16. Berry, B. S. Diffusion of carbon in nickel. *J. Appl. Phys.* **44**, 3792–3793 (1973).

476 17. Siegel, D. J. & Hamilton, J. C. First-principles study of the solubility, diffusion,
477 and clustering of C in Ni. *Phys. Rev. B* **68**, 094105 (2003).

- 478 18. Zhu, Y. A., Dai, Y. C., Chen, D. & Yuan, W. K. First-principles study of carbon
479 diffusion in bulk nickel during the growth of fishbone-type carbon nanofibers.
480 *Carbon* **45**, 21–27 (2007).
- 481 19. David, M., Prillieux, A., Monceau, D. & Connétable, D. First-principles study of
482 the insertion and diffusion of interstitial atoms (H, C, N and O) in nickel. *J. Alloys*
483 *Compd.* **822**, 153555 (2020).
- 484 20. Niu, Y. M. et al. Manipulating interstitial carbon atoms in the nickel octahedral
485 site for highly efficient hydrogenation of alkyne. *Nat. Commun.* **11**, 3324 (2020).
- 486 21. Wang, S. B., Lu, G. Q. & Millar G. J. Carbon dioxide reforming of methane to
487 produce synthesis gas over metal-supported catalysts: state of the art. *Energy Fuels*
488 **10**, 896–904 (1996).
- 489 22. Jabbour, K. Tuning combined steam and dry reforming of methane for “metgas”
490 production: A thermodynamic approach and state-of-the-art catalysts. *J. Energy Chem.*
491 **48**, 54–91 (2020).
- 492 23. Palmer, C. et al. Dry reforming of methane catalysed by molten metal alloys. *Nat.*
493 *Catal.* **3**, 83–89 (2020).
- 494 24. Jung, S., Lee, J., Moon, D. H., Kim, K. H. & Kwon, E. E. Upgrading biogas into
495 syngas through dry reforming. *Renewable Sustainable Energy Rev.* **143**, 110949
496 (2021).
- 497 25. Shoji, S. et al. Photocatalytic uphill conversion of natural gas beyond the
498 limitation of thermal reaction systems. *Nat Catal.* **3**, 148–153 (2020).
- 499 26. Song, H. W., Su, J. & Wang, C. X. Vacancies revitalized Ni₃ZnC_{0.7} bimetallic
500 carbide hybrid electrodes with multiplied charge-storage capability for high-capacity
501 and stable-cyclability lithium-ion storage. *ACS Appl. Energy Mater.* **1**, 5008–5015
502 (2018).

- 503 27. Umadevi, M., Bella, S. A. J. & Ramakrishnan, V. Raman spectral investigations
504 on the binary system (acetic acid N, N–dimethyl formamide). *J. Raman Spectrosc.* **38**,
505 231–238 (2007).
- 506 28. Piqué, O. et al. Subsurface carbon: a general feature of noble metals. *Angew.*
507 *Chem. Int. Ed.* **58**, 1744–1748 (2019).
- 508 29. Garcia–Ortiz, A. et al. Synthesis of a hybrid Pd⁰/Pd–carbide/carbon catalyst
509 material with high selectivity for hydrogenation reactions. *J. Catal.* **389**, 706–713
510 (2020).
- 511 30. Pan, L. et al. MOF–derived C–doped ZnO prepared via a two–step calcination for
512 efficient photocatalysis. *Appl. Catal. B: Environ.* **189**, 181–191 (2016).

513 **Acknowledgements**

514 The authors acknowledge the National Natural Science Foundation of China (Grant
515 Nos. 21878203, 21975174, 11934007, 11874194 and 51632005), the Program for the
516 Top Young and Middle-Aged Innovative Talents of Higher Learning Institutions of
517 Shanxi. Prof. X Yan would like to especially thank Dr. Ya Wang of Harbin
518 Engineering University for calculating the Gibbs free energy and Prof. Baojun Wang
519 of Taiyuan University of Technology for VASP support. The authors acknowledge the
520 SUSTech Core Research Facilities for the TEM instrument usage.

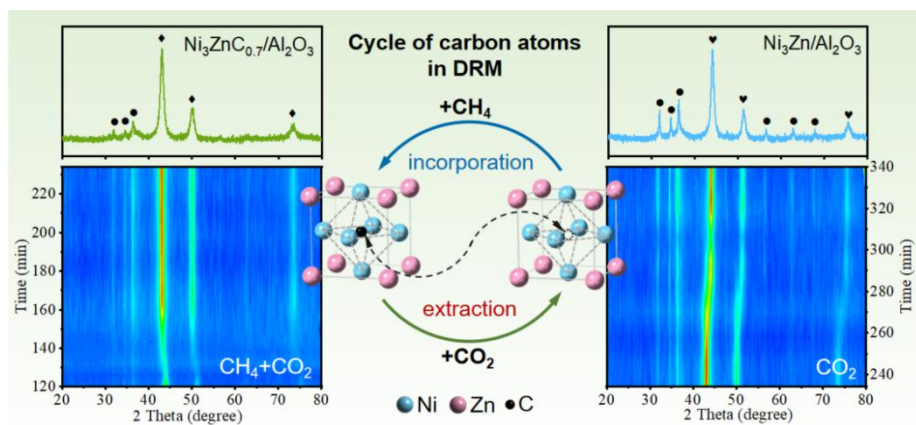
521 **Author contributions**

522 Q.W., S.L., X.Y. and R.L. conceived and designed the experiments. Q.W. and M.C.
523 prepared the materials, carried out the catalytic performance in DRM, and performed
524 the XRD, SEM, ICP-AES, Raman, TPSR–MS, elemental analysis. W.W. and J. H.
525 carried out TEM and in situ ETEM/EELS experiment and analysis. P.W. performed
526 the in situ XRD characterizations. Q.W. and X.Y. co-wrote the manuscript.

527 **Competing interests**

528 The authors declare no competing interests.

529 **Graphical abstract**



530

Supplementary Files

This is a list of supplementary files associated with this preprint. Click to download.

- [SupplementaryInformationforNatureCatalysis.docx](#)
- [SupplementaryMovie1.gif](#)